

# Parsimonious Bayesian sparse tensor regression using the Tucker decomposition

Daniel Spencer, Rajarshi Guhaniyogi, Raquel Prado

March 10, 2022

## Abstract

Tensors, or multidimensional data arrays, require dimension reduction in modeling applications due to their large size. In addition, these structures typically exhibit inherent sparsity, requiring the use of regularization methods to properly characterize an association between a covariate and a response. In this paper, we propose a Bayesian method to parsimoniously model a scalar response with a tensor-valued covariate using the Tucker tensor decomposition. This method retains the spatial relationship within a tensor-valued covariate, while reducing the number of parameters varying within the model and applying appropriate regularization methods. Simulated data are analyzed to demonstrate model effectiveness, with comparisons made to both classical and Bayesian methods. A neuroimaging analysis using data from the Alzheimer’s Data Neuroimaging Initiative is also included.

## 1 Introduction

Image analysis has become an important application area with the development of computer memory that allows for storing large datasets on local computing machines. Indeed, machine learning applications of image analysis are now present in many fields of research, such as medical imaging, character translation, and self-driving cars. In many of these cases, a linear model that provides inferential and/or prediction capabilities is all that is required. Such models have been shown to be very effective in settings with billions or trillions of observed data points. However, scenarios in which models are built on smaller sample sizes suffer from low sensitivity without imposing additional constraints or assumptions.

The field of medical imaging is particularly rich in methods dealing with large datasets and small sample sizes. Since its inception with the discovery of X-rays in 1895 [Bercovich and Javitt, 2018], the field has grown to be a major component of modern medicine. The digitization of medical imaging in recent decades has opened the doors to analysts outside the purview of local hospitals and radiology centers, lifting some of the burden of diagnosis from radiologists and reducing the rate of medical errors [Bruno et al., 2015]. This shift also allows researchers to develop new models that can provide insight into how bodily mechanisms

work inside living subjects by enabling the combined analysis over a number of subjects, improving statistical power. Due to the clinical importance of inference and prediction from these models, any assumptions and constraints must be carefully applied.

Several methods are already in use for these types of data within the neuroimaging community. One of the most commonly-used methods is referred to as the general linear model (GLM), which is not to be confused with the generalized linear model that is commonly used in statistics. This model performs a massive univariate analysis in which the response is regressed independently on each cell within a tensor covariate, in addition to any additional vector covariates [Friston et al., 1995, Penny et al., 2011]. These models have the advantage of being relatively computationally inexpensive and easily parallelizable. However, they also assume that the associations between different cells in the tensor and the response are all independent and not necessarily sparse. In practice, different multiple testing corrections are used to preserve spatial relationships among proximal cells via independent components analysis, though work by Eklund et al. [2016] suggests that these inflate the false discovery rate. Methods that control the false discovery rate are appealing [Benjamini and Hochberg, 1995, Lindquist and Mejia, 2015], but they fail to take spatial relationships within the tensor coefficient into account.

A different class of approaches takes advantage of the tensor structure of the data by decomposing the tensor covariates using one of two tensor decompositions and imposing regularization constraints. Work done by Zhou et al. [2013] uses the parallel factorization/canonical polyadic (PARAFAC/CP) tensor decomposition in a classical tensor regression approach, which assumes that dimension margins are principal components of the tensor coefficients. This was expanded in the work by Li et al. [2018] in the use of the more flexible Tucker decomposition. Guhaniyogi et al. [2017] created a novel Bayesian prior structure on the PARAFAC/CP tensor decomposition elements, which improved on the uncertainty quantification from the model inference.

In this article, we outline the Bayesian Tensor Regression with Tucker (BTRT) model that satisfies the careful implementation of assumptions of sparsity and spatial similarity within a tensor-valued coefficient. This is accomplished through the use of the Tucker tensor decomposition [Tucker, 1966], a more flexible extension of the PARAFAC/CP decomposition. In section 2, we outline the BTRT model and its competitors. In section 3, we show the efficiency and accuracy of the model over a number of competitors using simulated data. In section 4, the BTRT model and its competitors are applied in a neuroimaging analysis of data from the Alzheimer’s Disease Neuroimaging Initiative. Section 5 outlines our conclusions and possible research extensions.

## 2 Methodology

### 2.1 Tensor terminology and notation

Before proceeding to the linear model and prior structure in our proposal, the notation that will be used for tensor representations must be fully explained. The term *tensor* is a generalization of an arrayed data structure. A tensor of order  $D$  is a multi-dimensional array data structure  $\mathbf{B} \in \mathbb{R}^{p_1 \times \dots \times p_D}$ . Therefore, a vector is a tensor of order 1, a matrix is a tensor of order 2, a cubic array is a tensor of order 3, and so forth.

The *vectorization* of a tensor  $\mathbf{B} \in \mathbb{R}^{p_1 \times \dots \times p_D} : D \geq 2$  results in a tensor of order 1 of length  $\prod_{j=1}^D p_j$ , i.e.  $\text{vec}\mathbf{B} \in \mathbb{R}^{p_1 \dots p_D}$ . The *inner product* of two tensors  $\mathbf{A}$  and  $\mathbf{B}$  with the same dimensions is the crossproduct of the vectorized elements of the tensors, that is  $\langle \mathbf{A}, \mathbf{B} \rangle = (\text{vec}\mathbf{A})^T (\text{vec}\mathbf{B})$ .

The  $k$ th-mode *matricization* of a tensor, represented as  $\mathbf{B}_{(k)}$  is a matrix representation of a tensor of order 2 or higher such that the  $k$ th index becomes the first index and all other tensor indices are combined in order into a second index. That is,  $\mathbf{B}_{(k)} \in \mathbb{R}^{p_k \times p_1 \dots p_{k-1} p_{k+1} \dots p_D}$ .

Finally, tensors can be represented via different *tensor decompositions*. A common decomposition that is currently in use is the canonical decomposition/parallel factorization, also known as CANDECOMP/PARAFAC, or CP [Tucker, 1966]. This decomposition represents the tensor  $\mathbf{B}$  as

$$\mathbf{B} = \sum_{r=1}^R \boldsymbol{\beta}_{1,r} \circ \dots \circ \boldsymbol{\beta}_{D,r}, \quad (1)$$

in which  $\boldsymbol{\beta}_j \in \mathbb{R}^{p_j}$  is one of  $R$  principal components for the  $j$ th dimension of  $\mathbf{B}$ . Here,  $R$  is known as the *rank* of the CP decomposition. The  $\circ$  operator denotes the *outer product*. At each value of  $r \in \{1, \dots, R\}$ , the series of outer products  $\boldsymbol{\beta}_{1,r} \circ \dots \circ \boldsymbol{\beta}_{D,r}$  results in a  $D$ -dimensional tensor summand  $\mathbf{B}_r \in \mathbb{R}^{p_1 \dots p_D}$ . As the value of  $R$  increases, the resolution allowed by the CP decomposition improves. All tensors can conform to this CP decomposition for some appropriate rank  $R$ . In practice, low-rank decompositions have been found to be adequate to estimate sparse tensor coefficients with spatial dependence between neighboring locations. Using the CP decomposition reduces the parameter space for estimating  $\mathbf{B}$  from  $\prod_{j=1}^D p_j$  to  $R \sum_{j=1}^D p_j$ , which results in better accuracy detecting signal that is sparse and spatially dependent. However, it is possible that not all dimensions of a tensor require all  $R$  principal components in order to be faithfully represented by such a decomposition. In such cases, the CP decomposition is extended to the *Tucker decomposition*, which can be written as

$$\mathbf{B} = \sum_{r_1=1}^{R_1} \cdots \sum_{r_D=1}^{R_D} g_{r_1, \dots, r_D} \boldsymbol{\beta}_{1, r_1} \circ \cdots \circ \boldsymbol{\beta}_{D, r_D}, \quad (2)$$

where

$$(g_{1, \dots, 1}, g_{2, \dots, 1}, \dots, g_{R_1, \dots, R_D}) = \mathbf{G} \in \mathbb{R}^{R_1, \dots, R_D}$$

is the *core tensor* composed of elements, which assigns weights of importance to each of the  $\prod_{j=1}^D R_j$  tensor summands that compose the tensor  $\mathbf{B}$  [Tucker, 1966]. This representation is more flexible and parsimonious than the CP decomposition, as it allows for smaller ranks for dimension margins that exhibit fewer distinct nonzero volumes within the tensor. The parameter space for estimating  $\mathbf{B}$  can be reduced from  $R \sum_{j=1}^D p_j$  when using the CP decomposition to  $\sum_{j=1}^D R_j p_j$  with the Tucker decomposition. With these basic conventions, a linear model can be built using the Tucker decomposition that is parsimonious with regard to the parameter space.

## 2.2 Tucker Tensor Regression Model

Assuming a scalar response  $y_i$ , for  $i = 1, \dots, n$  and tensor- and vector-valued predictors,  $\mathbf{X}_i \in \mathbb{R}^{p_1 \times \cdots \times p_D}$  and  $\boldsymbol{\eta}_i \in \mathbb{R}^q$ , respectively, the observed linear model can be represented as

$$y_i = \langle \mathbf{B}, \mathbf{X}_i \rangle + \boldsymbol{\gamma}' \boldsymbol{\eta}_i + \epsilon_i, \quad (3)$$

in which  $\mathbf{B} \in \mathbb{R}^{p_1 \times \cdots \times p_D}$  is a tensor-valued coefficient,  $\boldsymbol{\gamma} \in \mathbb{R}^q$  is a vector-valued coefficient, and  $\epsilon_i$  is an error term, which follows any distribution centered at zero. Note that, since we are focusing on the methods to address tensor regression, we are restricting our attention to scenarios in which  $q$  is relatively small. However, the model framework here does allow for a seamless extension to a high-dimensional  $\boldsymbol{\eta}_i$ .

Given the potentially large predictor space within the tensor-valued covariate, it is reasonable to assume that some cases exist in which the association between the elements in  $\mathbf{X}_i$  and  $y_i$  is sparse. In order to include this structure into the model while simultaneously reducing the parameter space, the Tucker tensor decomposition is used, as outlined in (2). Furthermore, in order to impose strict, explicit constraints on the structure of the parameters in (3), Bayesian modeling is used. Specialized priors are imposed to induce sparsity on the estimates of the elements in  $\mathbf{B}$ , while standard Bayesian modeling techniques are applied to the  $\boldsymbol{\gamma}$  and  $\epsilon_i$  terms, as outlined below.

## 2.3 Prior structure

A key goal of the model is to address assumed sparsity in the tensor-valued coefficient. Classical regularization methods used to meet such a goal include various penalized regression algorithms like the LASSO [Tibshirani, 1996]. However, these methods lack the ability to provide a measure of uncertainty quantification on the estimates for the parameters. Shifting to a Bayesian modeling structure can serve to fill this gap, leading to improved inference in some cases.

Li et al. [2018] proposes a classical model for tensor regression using the Tucker decomposition in which a penalty is applied to either the core tensor  $\mathbf{G}$  or both the core tensor  $\mathbf{G}$  and each dimension component  $\beta_{j,r_j}$  in the decomposition. We propose shrinkage priors on both the core tensor and all dimension components in order to more strongly induce parameter regularization.

Following the previous work done by Guhaniyogi et al. [2017], an adapted generalized double-Pareto prior is applied to the dimension components within the Tucker tensor decomposition. That is,

$$\begin{aligned}\beta_{j,r_j} &\sim \text{Normal}(\mathbf{0}, \tau \mathbf{W}_{j,r_j}), \\ \tau &\sim \text{Gamma}(a_\tau, b_\tau), \\ \omega_{j,r_j,\ell} &\sim \text{Exponential}\left(\frac{\lambda_{j,r_j}^2}{2}\right), \\ \lambda_{j,r_j} &\sim \text{Gamma}(a_\lambda, b_\lambda),\end{aligned}$$

where  $\mathbf{W}_{j,r_j}$  is a diagonal matrix with elements  $\omega_{j,r_j,\ell}$  for  $\ell = 1, \dots, p_j$ . Integrating over the element-specific scale parameters reduces the prior on  $\beta_{j,r_j,\ell}$  to a double-exponential distribution centered at 0 with a scale parameter of  $\frac{\lambda_{j,r_j}}{\sqrt{\tau}}$ , which has heavier tails than a Gaussian distribution, while also allocating higher densities around zero. This produces an analog to the adaptive LASSO, including its desirable oracle properties of the maximum a posteriori estimator [Armagan et al., 2013].

In order to adequately select the proper rank for each dimension and to reduce noise in the tensor coefficient estimates, the generalized double-Pareto prior is also imposed on the elements of the core tensor  $\mathbf{G}$ :

$$\begin{aligned}
g_{r_1, \dots, r_D} &\sim \text{Normal}(0, z v_{r_1, \dots, r_D}) \\
z &\sim \text{Gamma}(a_z, b_z) \\
v_{r_1, \dots, r_D} &\sim \text{Exponential}\left(\frac{\varphi_{r_1, \dots, r_D}^2}{2}\right) \\
\varphi_{r_1, \dots, r_D} &\sim \text{Gamma}(a_\varphi, b_\varphi)
\end{aligned}$$

This combination ensures that only summands within the Tucker decomposition that explain additional variance are included in the model. Selection of important ranks can be done using the sequential 2-means post-hoc variable selection procedure proposed by Li and Pati [2017].

For the purposes of the analyses in this article, a multivariate normal prior with mean  $\boldsymbol{\mu}_\gamma$  and covariance  $\boldsymbol{\Sigma}_\gamma$  is placed on the elements of  $\gamma$ . This is done to maintain conjugacy while maintaining control over the expected effects of the vector-valued coefficients. The errors ( $\epsilon_i$ ) in this model are assumed to be independent and identically distributed following a normal distribution with a mean of zero, and a variance of  $\sigma_y^2$ . An inverse gamma prior is placed on  $\sigma_y^2$  with hyperparameters  $a_\sigma$  and  $b_\sigma$ .

$$\begin{aligned}
\gamma &\sim \text{Normal}(\boldsymbol{\mu}_\gamma, \boldsymbol{\Sigma}_\gamma) \\
\epsilon_i &\stackrel{i.i.d.}{\sim} \text{Normal}(0, \sigma_y^2) \\
\sigma_y^2 &\sim \text{Inverse Gamma}(a_\sigma, b_\sigma)
\end{aligned}$$

## 2.4 Identifiability

The decomposition of the tensor coefficient raises questions about the identifiability of the parameters in the model. That is, if the value of any cell within the tensor coefficient is estimated as

$$\hat{b}_v \in \hat{\mathbf{B}} : \hat{b}_v = g_{1, \dots, 1} \beta_{1, 1, v_1} \cdots \beta_{D, 1, v_D} + \dots + g_{R_1, \dots, R_D} \beta_{1, R_1, v_1} \cdots \beta_{D, R_D, v_D},$$

where  $v$  is the cell location within the tensor ( $v = (v_1, \dots, v_D)$ ), then any two of these summands can be multiplied by  $c$  and  $\frac{1}{c}$ , respectively for some constant  $c$ , and the estimate for that cell within the tensor coefficient  $\hat{b}_v$  would have the same value. Indeed, the values of  $g_{r_1, \dots, r_D}$  and  $\beta_{j, r_j, v_j}$  are not identifiable, but  $\hat{b}_v$  remains identifiable through the shrinkage priors on the tensor decomposition components.

Something to consider when using this model for a data analysis is that an identifiability problem exists between  $\mathbf{B}$  and  $\gamma$  if there are cells within  $\mathbf{X}$ ,  $\forall i = 1, \dots, n$  that are collinear with any of the values in

$\boldsymbol{\eta}$ ,  $\forall i = 1, \dots, n$ . This is a problem that may go undetected in two-step frequentist models with regularization, as either elements in  $\mathbf{B}$  or  $\boldsymbol{\gamma}$  may simply be assigned values of zero.

## 2.5 Selection of Rank

A key consideration in the use of the proposed model structure is the selection of each dimension rank. Increases in a margin's rank can be made with an attempt to increase the spatial resolution on the inference of the tensor coefficient. For larger tensor covariates, this may require higher ranks than smaller tensors if the nonzero coefficients are not hypercubic. Choice of unequal ranks may be prudent if some of the tensor dimensions are much larger or smaller than others. Consider an example in which the tensor covariate has dimensions  $100 \times 100 \times 4$ . The ranks for the first two dimensions may need to be considerably larger than the rank for the final dimension, as there are only four possible margin locations in the final dimension. One such realistic application would be to combine magnetic resonance images that use different sequences (e.g. T1 weighted, T2 weighted, effective T2, etc.) into a single tensor, using a low rank on the dimension that represents different sequences. This is a clear advantage over the CP/PARAFAC decomposition methods, as each dimension is not forced to have the same number of ranks as all of the others.

Once a set of reasonable ranks is decided for each tensor dimension, the different combinations of the ranks should be used to fit models and compare results using some model selection criterion like the DIC.

## 2.6 Competitor Models

The effectiveness of the proposed Bayesian sparse tensor regression models is shown by making direct comparisons to models commonly used in the field of neuroscience. The first is the general linear model (GLM), in which the response  $(y_1, \dots, y_n) = \mathbf{y}$  is regressed on each cell  $v$  within the tensor covariate  $\mathbf{X} \in \mathbb{R}^{p_1, \dots, p_D}$  independently with the vector-valued coefficients. The linear model for the GLM is written in equation (4). Note that the same responses  $(y_1, \dots, y_n) = \mathbf{y}$  are used to fit separate models for each cell within the tensor covariate.

$$y_i = b_v X_{i,v} + \boldsymbol{\gamma}' \boldsymbol{\eta}_i + \epsilon_{i,v} \quad (4)$$

This model is an industry standard for its ease of implementation and rapid completion. However, this model often suffers from a high false discovery rate [Eklund et al., 2016], and does not provide a single estimate for the vector-valued coefficient. We adjust for the high false discovery rate in our implementation by using the Benjamini-Hochberg multiple testing correction [Benjamini and Hochberg, 1995], which fixes the false discovery rate (FDR). In the following trials, the FDR is fixed at 0.05, in agreement with standard practice

in neuroimaging. In order to provide a single estimate for the vector of coefficients  $\gamma$ , a two-step GLM algorithm could be used, which is described in algorithm 1. In the implementation of these models,  $\delta$  is set to be equal to 1.

---

**Algorithm 1:** Two-step method for regressing response  $\mathbf{y}$  on vector-valued covariates  $\boldsymbol{\eta}$  and tensor-valued covariates  $\mathbf{X}$ .

---

**Result:** Estimates of  $\gamma$  and  $\mathbf{B}$

- 1 Initialize  $\gamma^{(0)}$  as  $\max_{\gamma} \ell(\mathbf{y}, \boldsymbol{\eta}, \gamma)$ ,  $\mathbf{B}^{(0)}$  as  $\max_{\mathbf{B}} \ell(\mathbf{y}, \boldsymbol{\eta}, \mathbf{X}, \gamma^{(0)}, \mathbf{B})$ ;
- 2 **repeat**
- 3     Set  $\gamma^{(t+1)} = \max_{\gamma} \ell(\mathbf{y}, \boldsymbol{\eta}, \mathbf{X}, \gamma, \mathbf{B}^{(t)})$ ;
- 4     Set  $\mathbf{B}^{(t+1)} = \max_{\mathbf{B}} \ell(\mathbf{y}, \boldsymbol{\eta}, \mathbf{X}, \gamma^{(t+1)}, \mathbf{B})$ ;
- 5 **until**  $\max(\max(\mathbf{B}^{(t+1)} - \mathbf{B}^{(t)}), \max(\gamma^{(t+1)} - \gamma^{(t)})) < \delta$ ;

---

The advantage of the two-step GLM is that it produces single estimates of  $\gamma$ , and as a result, tends to have a lower FDR. Here again, the Benjamini-Hochberg multiple testing correction is used to limit the false discovery rate in deciding which cells in the tensor coefficient are significantly different from zero.

Direct tensor regression competitors are also used to validate the performance of the proposed model structure. Specifically, the frequentist tensor regression using the PARAFAC/CP tensor decomposition [Zhou et al., 2013] and the Tucker tensor decomposition [Li et al., 2018] are used to compare point estimates to classical methods. Comparison to the Bayesian tensor regression using the PARAFAC/CP tensor decomposition [Guhaniyogi et al., 2017] provides a more direct comparison in terms of point estimates and uncertainty quantification.

### 3 Simulated Data Analysis

On order to demonstrate the efficacy of the proposed Bayesian model, data were simulated from the linear model in (3) under the conditions  $\mathbf{B} \in \mathbb{R}^{50 \times 50}$ , where nonzero-valued elements take the value of 1 in the middle of the regions, fading outward to lower positive values using the `specifyregion` function within the `neuRosim` package in R [Welvaert et al., 2011]. For the sake of these simulations, three separate regions of activation are generated at random locations. The elements of  $\mathbf{X}_i$  are all independently generated from a standard normal distribution for  $i = 1, \dots, 1000$ . The elements for the vector-valued covariates  $\boldsymbol{\eta}_i$  are also independently generated from a standard normal distribution. The parameters for the vector-valued covariates are set as  $\gamma = (\gamma_1, \gamma_2, \gamma_3) = (25, 3, 0.1)$  to show how the different models estimate parameters of different size, relative to the observation error, which is set to have a variance of 1. Finally, the elements of  $\mathbf{y} = (y_1, \dots, y_n)$  are generated according to (3) for  $\epsilon_i \sim \text{Normal}(0, 1)$ .

The Bayesian models had the following hyperparameter settings:  $a_\sigma = 3$ ,  $b_\sigma = 20$ ,  $a_\lambda = 3$ ,  $b_\lambda = a_\lambda^{1/(2D)}$ ,  $\boldsymbol{\mu}_\gamma = \mathbf{0}$ ,  $\boldsymbol{\Sigma}_\gamma = 900\mathbf{I}_q$ ,  $a_\tau = 1$ ,  $b_\tau = \min(R_1, \dots, R_D)^{(1/D)-1}$ ,  $a_z = 1$ ,  $b_z = \min(R_1, \dots, R_D)^{(1/D)-1}$ ,  $a_\varphi = 3$ , and  $b_\varphi = a_\varphi^{1/(2D)}$ . The prior on the observation error variance is set to be relatively noninformative in the context of the simulation, with a mean of 10 and a variance of 100. The priors for  $\lambda$  and  $\varphi$  are set to have modes between 1.5 and 2, getting closer to 2 as the tensor dimension increases, which places the prior expected value for  $v_{r_1, \dots, r_D}$  and the elements within  $\mathbf{W}_{j, r_j}$  to be between  $\frac{2}{3}$  and  $\frac{1}{2}$ . The priors for  $\tau$  and  $z$  have a mean of 1 when all  $R_1, \dots, R_D = 1$ , increasing sublinearly with both the minimum value of  $R_j$  for  $j = 1, \dots, D$ , and the tensor dimension  $D$ . The prior variance for  $\tau$  and  $z$  increases linearly in rank when  $D = 2$ , and superlinearly in rank when  $D > 2$ . This prior specification allows for a slightly higher prior variance for  $\beta_{j, r_j}$  and  $g_{r_1, \dots, r_D}$  as rank and dimension increase in order to allow for moderately faster exploration of the parameter space as the tensor dimension and rank increase. The prior for  $\gamma$  is set to be relatively noninformative, with means at 0, standard deviations of 30, and assumed independence.

For all 16 models with  $R_1, R_2 \in \{1, 2, 3, 4\}$ , 11,000 Markov Chain Monte Carlo (MCMC) simulations from the posterior distribution were drawn. After discarding the first 1000 draws, the remaining draws were used to estimate  $\mathbf{B}$  and  $\gamma$ .

Since the model does not produce exact zeros as estimates for zero-valued parameters, the sequential 2-means variable selection method proposed by Li and Pati [2017] is used for variable selection within the tensor coefficient. The method works by using 2-means clustering of any subset of the parameter space on the absolute values of each draw from the posterior distribution. The number of values in the cluster in which the center is furthest from zero is taken as the number of nonzero-valued parameter estimates for that particular posterior sample. The median number of non-zero parameter estimates across all of the posterior samples,  $m$  is then found. Finally, the parameters with the  $m$  highest posterior median absolute values are determined to have true non-zero values. These parameters are then estimated with their posterior medians.

This process is formally described in algorithm 2.

---

**Algorithm 2:** Sequential 2-means for posterior draws  $s = 1, \dots, S$  for parameter  $\theta$

---

**Result:** Final estimate of  $\theta$  with small elements set to be equal to 0

```

1 for  $s \leftarrow 1$  to  $S$  do
2   Cluster the absolute value of elements in  $\theta^{(s)}$  into two clusters,  $\mathcal{A}$  and  $\mathcal{B}$ , where  $\bar{\mathcal{A}} \leq \bar{\mathcal{B}}$ , where  $\bar{\mathcal{A}}$  and  $\bar{\mathcal{B}}$  denote the mean of elements in the clusters  $\mathcal{A}$  and  $\mathcal{B}$  respectively;
3   Cluster the elements of  $\mathcal{A}$  into two clusters,  $\mathcal{A}$  and  $\mathcal{A}'$  such that  $\bar{\mathcal{A}} < \bar{\mathcal{A}'}$ ;
4   while  $|\bar{\mathcal{A}} - \bar{\mathcal{A}'}| > b$  do
5     Cluster the elements of  $\mathcal{A}$  into two clusters,  $\mathcal{A}$  and  $\mathcal{A}'$  such that  $\bar{\mathcal{A}} < \bar{\mathcal{A}'}$ ;
6   end
7   The number of elements remaining in  $\mathcal{A}$  is the estimated number of true zero-valued elements,
8    $n_z^{(s)}$ , in  $\theta^{(s)}$ 
9 end
10 Find  $\hat{n}_z = \text{median value of } n_z$  ;
11 Find  $\hat{\theta} = \text{median values of the elements in } \theta^{(1:S)}$  ;
12 Set elements in  $\hat{\theta}$  with the  $\hat{n}_z$  smallest absolute values to 0

```

---

Point estimates for the Bayesian and frequentist sparse Tucker tensor regression and the Bayesian and frequentist sparse CP tensor regression can be seen in Figure 1. In the interest of clarity, the only Tucker decomposition models shown are the equivalents to the PARAFAC/CP models. It is worth noting that additional ranks are needed in order to accurately detect additional nonzero regions in the true coefficient tensor. The Bayesian methods using the CP/PARAFAC decomposition do not exhibit the same gains in nonzero region detection as the Tucker decomposition models. All of the tensor regression methods show significant improvement over the two-step GLM competitor. In order to choose between the models, the deviance information criterion is used for the Bayesian sparse tensor regression models, while the log-likelihood is used for the frequentist sparse tensor regression models. The point estimates from these selected models, along with the two-step GLM estimate and the true values are shown in figure 2. The estimate shown for the two-step GLM tensor coefficient assigns values of zero to cells within the tensor that are not statistically significant after using the Benjamini-Hochberg multiple testing correction.

In order to compare the performance of these models, the root mean squared error (RMSE) for each element within  $\mathbf{B}$  can be compared in Table 2. Explicitly, the RMSE was found as  $\sqrt{\frac{1}{V} \sum_v (\hat{B}_v - B_v)^2}$ , where  $\hat{B}_v$  is the point estimate for tensor coefficient element  $v$  obtained from a model,  $B_v$  is the true value taken by the coefficient tensor element  $v$ , and  $V$  is the total number of elements in the coefficient tensor. These results show the effectiveness of the Bayesian sparse Tucker tensor regression model in estimating

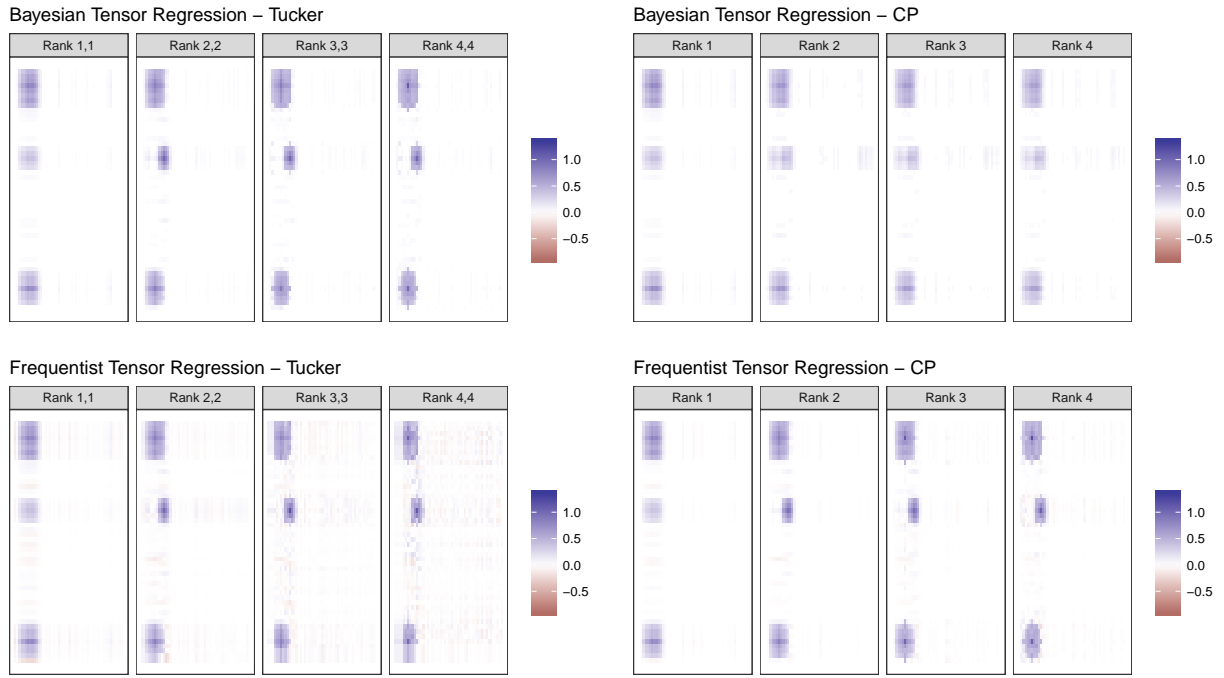


Figure 1: Point estimates of the true tensor coefficient for the Bayesian sparse Tucker tensor regression and the frequentist sparse Tucker tensor regression. The Bayesian point estimate was found using the sequential 2-means posterior variable selection method [Li and Pati, 2017].

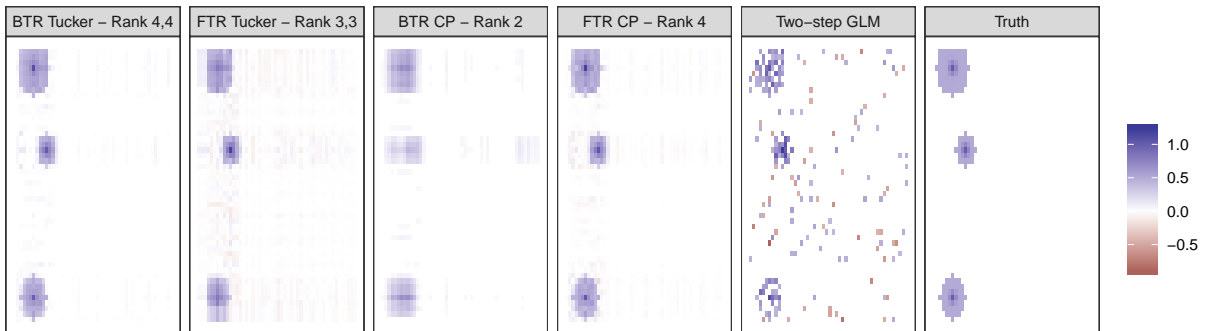


Figure 2: Point estimates of the true tensor coefficient for all competitors. Bayesian models were chosen using the deviance information criterion, and the frequentist models were chosen using the log-likelihood.

$R_1/R_2$	True Zero			
	1	2	3	4
1	0.955	0.955	0.955	0.955
2	0.955	0.965	0.965	0.966
3	0.959	0.966	0.968	0.970
4	0.959	0.965	0.971	0.975
	Rank 1	Rank 2	Rank 3	Rank 4
BTR CP	0.968	0.991	0.994	0.998
$R_1/R_2$	True Nonzero			
	1	2	3	4
1	0.391	0.384	0.391	0.404
2	0.391	0.503	0.503	0.503
3	0.404	0.503	0.669	0.656
4	0.391	0.503	0.642	0.735
	Rank 1	Rank 2	Rank 3	Rank 4
BTR CP	0.464	0.603	0.636	0.695

Table 1: Coverage probabilities of the 95% credible intervals for the true zero and true nonzero values within  $\mathbf{B}$  for different rank models.

true tensor coefficient values, exhibiting a lower RMSE than other tensor regression methods using tensor decompositions. In particular, significant improvements are seen over the Bayesian CP/PARAFAC models when both  $R_1$  and  $R_2$  are greater than 1. This is also visible in figure 1, where the gain in the true image recovery is much greater going from a rank 1,1 to rank 2,2 model than it is in the Bayesian CP/PARAFAC models going from Rank 1 to Rank 2. In addition, all of the competitor methods perform significantly better than the two-step GLM model, which is often used in neuroimaging studies.

The posterior densities for  $\{\gamma_1, \gamma_2, \gamma_3\}$  under different models can be seen in Figure 3. These results show that the posterior densities for each  $\gamma_j$  are centered at or around the true values. When a coefficient is very far from zero relative to the error in the likelihood distribution, as in the first column of plots in figure 3, the Bayesian models do show the effect of choosing a prior mean of 0. This inference would be improved by choosing prior mean values that more accurately reflect what is expected to be seen within the data, but the effect of this poorly specified prior are not extreme. However, when the true value is very close to zero, as in the last column of plots in figure 3, the Bayesian models still have high posterior densities above 0, suggesting that they do detect the weak signal for a small true coefficient value. Interestingly, the Bayesian sparse Tucker tensor regressions show much higher posterior densities around the true coefficient values in all cases. This is an effect of the improved inference estimating  $\mathbf{B}$ .

### 3.1 Model Convergence

In all Bayesian modeling settings, it is important to ensure that the MCMC converges around an area within the neighborhood of the global posterior mode. Given that the posterior inference matches the inference

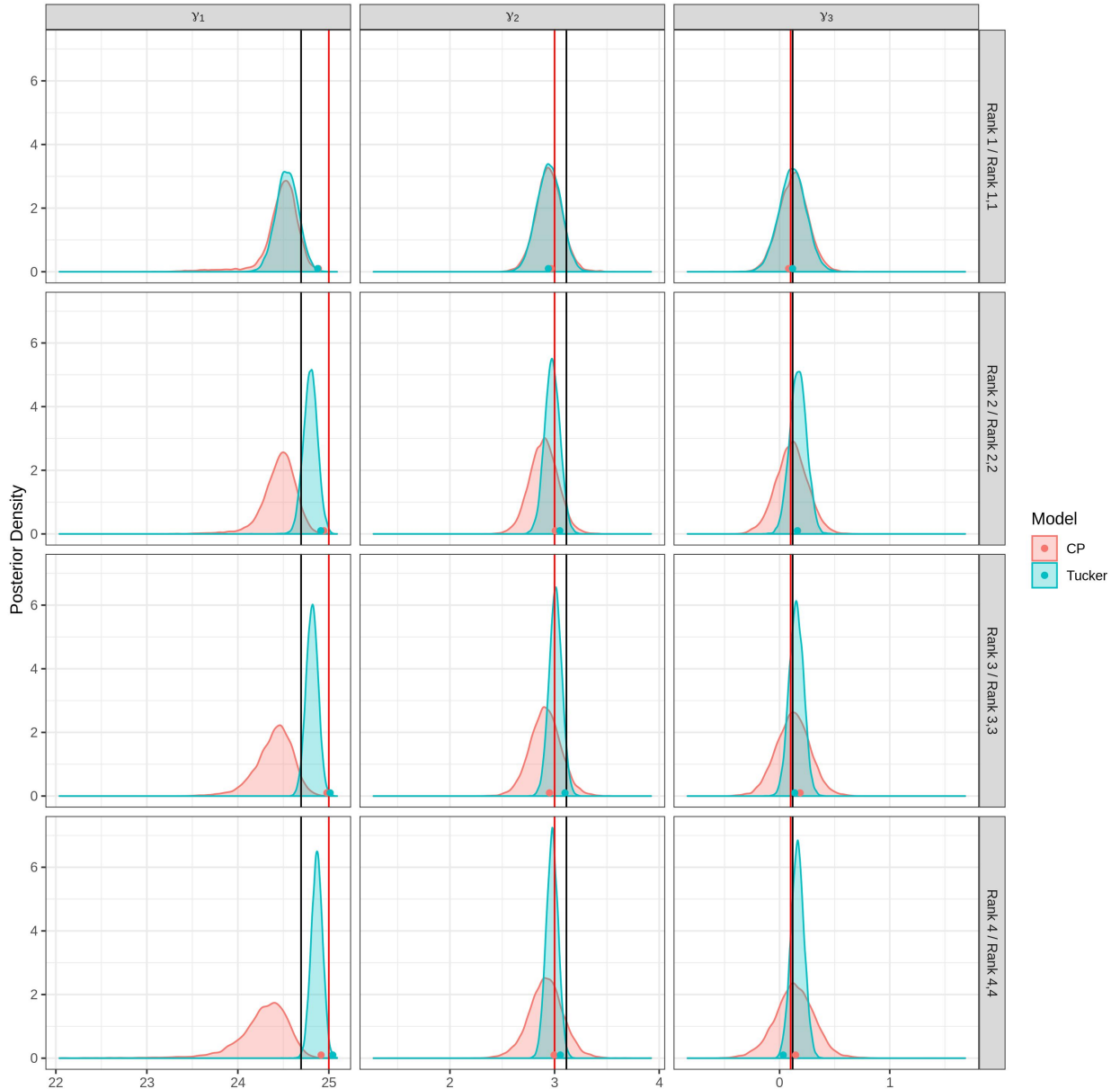


Figure 3: Posterior densities for  $\{\gamma_1, \gamma_2, \gamma_3\}$  under different models. Points indicate the estimates from the frequentist sparse tensor regression models. The red line indicates the true value, and the black line indicates the estimate from the two-step GLM frequentist model.

		BTR Tucker			
		1	2	3	4
$R_1/R_2$	1	0.0686	0.0686	0.0686	0.0686
	2	0.0686	0.0413	0.0413	0.0413
	3	0.0686	0.0413	0.0330	0.0330
	4	0.0687	0.0413	0.0330	0.0276
		FTR Tucker			
$R_1/R_2$	1	0.0718	0.0697	0.0719	0.0752
	2	0.0711	0.0467	0.0488	0.0544
	3	0.0719	0.0475	0.0501	0.0591
	4	0.0725	0.0491	0.0506	0.0617
		CP/PARAFAC			
Model	Rank 1	Rank 2	Rank 3	Rank 4	
	BTR	0.0690	0.0614	0.0614	0.0633
FTR	FTR	0.0686	0.0420	0.0383	0.0297
	GLM	<u>No Ranks</u>		0.1355	

Table 2: The root mean squared error (RMSE) for the estimates of  $\mathbf{B}$  under Bayesian sparse tensor regression (BTR) and frequentist sparse tensor regression (FTR) using the Tucker and CP tensor decompositions. The RMSE for the general linear model (GLM) is provided as a comparison.

shown within the frequentist models, the model does converge to a global mean in the simulated data settings when the assumption of normal error is satisfied, and the prior distributions are specified to be relatively uninformative. The log-likelihoods, shown in Figure 4, also show rapid convergence to a mode and posterior stability.

### 3.2 Hyperparameter Sensitivity

Modeling in such a high-dimensional space with several hierarchical levels in the prior structure requires careful selection of hyperparameter values. However, the model is still expected to be somewhat robust to differences in prior specification. In order to test this expectation, a large grid of hyperparameter values for  $a_\sigma, b_\sigma, a_\lambda, a_\tau, a_z$ , and  $a_\varphi$  was created. First, the values for the hyperparameters used to model the simulated data are taken and multiplied by 0.1, 1, or 10. One hundred configurations were randomly selected from the 729 possible configurations, and the model with ranks  $R_1 = R_2 = 3$  was run with the same simulated data as above for 11,000 iterations with each combination. In each case, 1,000 iterations in the MCMC were discarded as a burn-in.

Of the 100 configurations, 93 converged to have an RMSE for the tensor coefficient  $\mathbf{B}$  between 0.03279 and 0.03336. The remaining 7 configurations all had RMSEs within  $10^{-8}$  of 0.1336523, which is the RMSE

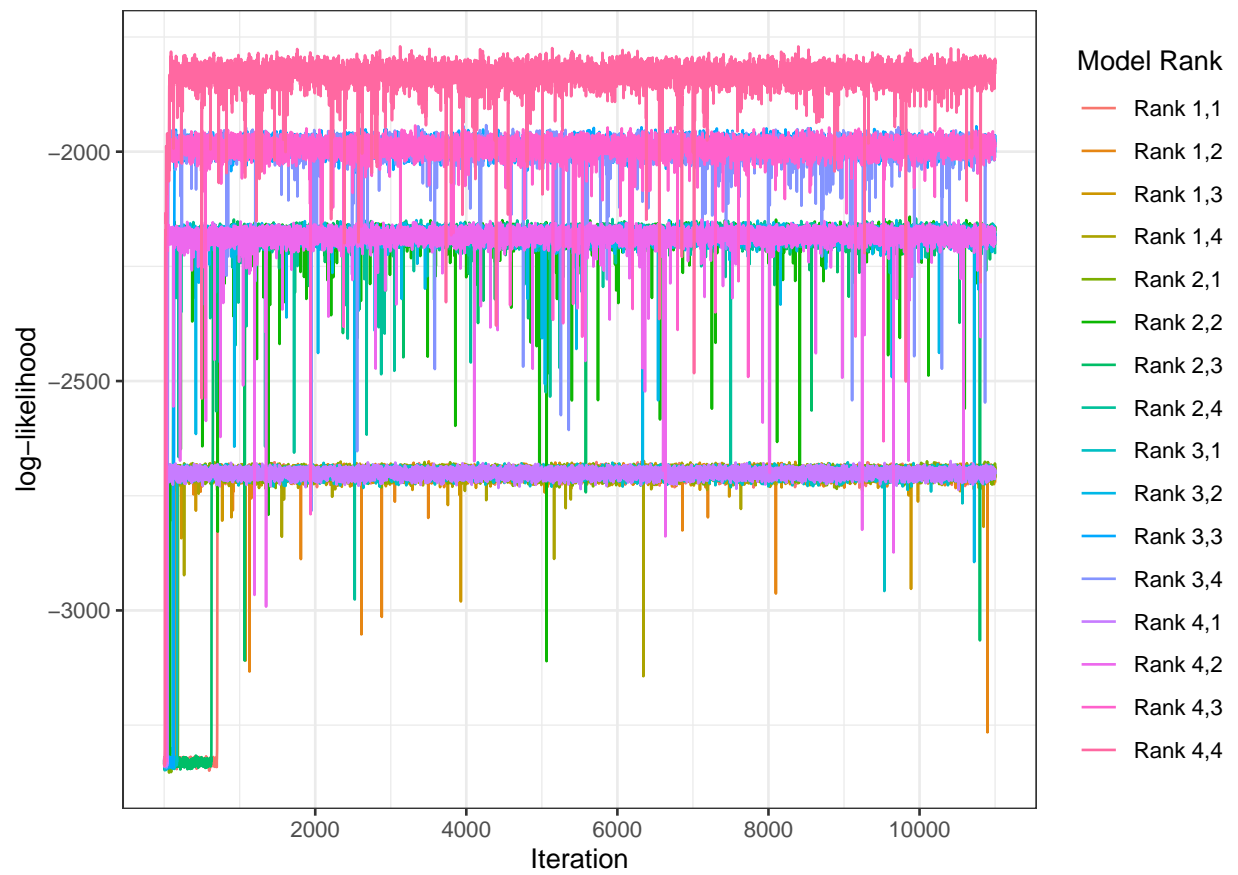


Figure 4: The log-likelihoods for the models applied to the simulated data

that results from predicting  $\mathbf{B}$  with a tensor of all zeros. The priors for these seven configurations all had the smallest values for the prior variance for the elements of  $\mathbf{B}$  (approximately  $2 \times 10^{-3}$ ) and/or the highest prior means (approximately  $10^{10}$ ) and variances (over  $10^{20}$ ) for  $\sigma_y^2$ . Indeed, individual inspection of these models with larger RMSE values show that the estimates for  $\gamma$  are within the same range as the estimates from the models that had a lower RMSE for the tensor coefficient, but they all estimate that the tensor coefficient is zero. This highlights the need to carefully balance the amount of shrinkage that can be applied to elements within  $\mathbf{B}$  before no image coefficients are recovered. In addition, the prior specification for  $\sigma_y^2$  must be reasonable in order to achieve interpretable results.

## 4 Neuroimaging Analysis

Data from magnetic resonance images (MRIs) of the brain have been found to have sparse, spatially-contiguous associations with certain phenotypes, such as cognitive performance scores or neurological disorders. In order to demonstrate the efficacy of the Bayesian sparse Tucker tensor regression, data from the Alzheimer’s Disease Neuroimaging Initiative (ADNI) database ([adni.loni.usc.edu](http://adni.loni.usc.edu)) were used. The ADNI was launched in 2003 as a public-private partnership, led by Principal Investigator Michael W. Weiner, MD. The primary goal of ADNI has been to test whether serial magnetic resonance imaging (MRI), positron emission tomography (PET), other biological markers, and clinical and neuropsychological assessment can be combined to measure the progression of mild cognitive impairment (MCI) and early Alzheimer’s disease (AD). For these analyses, data from the “ADNI1: Complete 1 Yr 1.5T” image collection were used. The phenotype data “AD Challenge Training Data: Clinical (Updated)” were used in order to maintain consistency with a series of challenges put forth by ADNI in 2014. The AD challenge invited researchers and analysts from all over the world to use statistics and machine learning methods to try to address one of three subchallenges. Subchallenge 3 had the stated goal to “Classify individuals into diagnostic groups using MR imaging.” This can be done either by predicting the Mini-Mental State Exam (MMSE) or by using a classification model, such as binomial or multinomial logistic regression models.

The MMSE is a diagnostic tool used to classify adults based on levels of cognitive impairment [Pangman et al., 2000]. The exam itself poses a series of questions to test the subject’s ability to perform everyday tasks. The maximum score that one can achieve on the test is 30, and the scores take integer values. These scores can then be used in conjunction with other information to diagnose an individual. In both the training and test samples used within this analysis, scores ranged from 20 to 30.

The challenge was judged based on correlations between actual and predicted MMSE scores, which motivated the choice to model with the MMSE as the response variable. More specifically, our analysis used

the centered MMSE scores as the response  $\mathbf{y} = (y_1, \dots, y_n) = (\text{MMSE}_1, \dots, \text{MMSE}_n) - \overline{\text{MMSE}}$ , where  $\overline{\text{MMSE}}$  is the average MMSE score. This centering was done in both the training and testing datasets so that an intercept term would not need to be estimated, which could cause identifiability problems with the other non-tensor coefficients in the model. All data were accessed on September 30, 2019. For subjects with multiple scans within the dataset, the scan used was matched to the scan referenced within the ADNI data table found within the file `ADNI_Training_Q3_APOE_CollectionADNI1Complete 1Yr 1.5T_July22.2014.csv`, distributed on the ADNI website.

Brain extraction was performed on the downloaded scans using the `fsl_bet` function from the `fslr` package in R [Muschelli et al., 2015, robust automated brain extraction Smith, 2002]. Finally, affine linear registration to the MNI152 2mm T1-weighted brain template was done using the `flirt` function from the `fslr` package in R [Muschelli et al., 2015, Jenkinson and Smith, 2001, Jenkinson et al., 2002]. After these functions were performed, some scans needed to be removed from the sample, as not all of the scans in the dataset were properly labeled to orient the structural scan within the neuroimaging software. The result was a total of 403 usable structural scans that matched to subjects within the ADNI dataset. From these subjects, 303 were randomly assigned to a training dataset, and 100 were assigned to a test dataset. This resulted in a training dataset with 172 males and 131 females, with a mean age of 76.01 years and standard deviation of 6.68 years, mean education level of 15.42 years and standard deviation of 3.04 years, and mean MMSE score of 27.03 and a standard deviation of 2.47. The testing dataset had 60 males and 40 females, with a mean age of 75.49 years and standard deviation of 6.61 years, mean education level of 16.00 years and standard deviation of 2.91 years, and mean MMSE score of 26.65 and standard deviation of 2.84. Since Alzheimer's disease (AD) is found to be significantly associated with larger ventricular volume in the brain, [Nestor et al., 2008], the 45th axial slice was chosen for analysis. Since the ventricles are filled with fluid rather than white matter from the brain, a positive association with the MMSE scores in the region of the ventricles would be consistent with the results of Nestor et al. [2008]. The selected axial slice contains ventricular volume in healthy adults, which would be expected to expand at a faster rate with age in adults with Alzheimer's disease. The values within each subject's image slice had the mean value for the nonzero tensor covariate cells subtracted from it, and then was divided by the standard deviation of that subject's nonzero cells to remove any subject-specific effect in terms of the unitless measure from the scanner. Finally, the parts of the axial slice that fell outside the brain region within the template were removed from the covariate tensor in order to try to improve the coefficient estimation. This resulted in a tensor covariate for each subject  $\mathbf{X}_i \in \mathbb{R}^{70 \times 87}$ .

For the non-tensor covariates in each subject,  $\boldsymbol{\eta}_i$ , the number of years of education and the number of Apolipoprotein E4 (APOE4) alleles present in a subject's DNA (0, 1, or 2). The number of years of

education shows a significant association with the MMSE scores in an exploratory data analysis. APOE4 has been identified as a genetic risk factor for Alzheimer’s disease [Strittmatter and Roses, 1996]. The APOE4 covariate was treated as continuous, as exploratory data analysis suggests a linear association with the MMSE.

For the comparison of models in these scenarios, the root mean squared predictive error and the Pearson correlation between the predictions and the actual values in the test dataset are used. The Pearson correlation is included because it was used as a performance metric in the DREAM challenge. Each Bayesian model is run for 11,000 iterations, after which 1,000 iterations are discarded as a burn-in. The frequentist tensor regression models are run until the log-likelihood change between steps is less than 0.1.

Final estimates for the tensor coefficient are found in the Bayesian models by using the sequential 2-means post-hoc variable selection method. The frequentist tensor regression models are not corrected, as they use the LASSO to select the coefficients that are significantly different from zero. The two-step GLM model estimate is found by applying the Benjamini-Hochberg multiple testing correction and setting cells that are not significant to have values of zero. The deviance information criterion is used to select which Bayesian model should be used to fit the data, and the Bayesian information criterion is used to select the frequentist rank models. The plots for the final estimates can be seen in Figure 5. These estimates are very different among the different models, which may suggest that there is very low signal within these data to conclude that there are nonzero coefficient values. Nonetheless, the point estimate from the BTR Tucker model shows some positive associations along the medial wall and left posterior ventricle, which is consistent with studies that show that increased ventricle volume is associated with Alzheimer’s disease [Nestor et al., 2008], and thus, the MMSE. Point estimates for the non-tensor coefficients ( $\gamma$ ) were found as the posterior medians in the Bayesian models after the burn-in. The estimates from the selected competitor models can be seen in table 3, along with the 95% posterior credible intervals for the Bayesian models.

In order to further verify the fits of the models, the model fits to the training data are used to predict the MMSE values in the test dataset. The Bayesian models produce predictions as the means of their posterior predictive distributions. The two-step GLM results are used to predict after the Benjamini-Hochberg multiple testing correction is applied to the tensor coefficient. That is, any cells within the tensor coefficient that are not deemed to be statistically significant are assigned a value of zero. The frequentist tensor regression models do not have any multiple testing correction applied, due to their use of the LASSO. For comparison, the root mean squared predictive error and the Pearson correlation are calculated for each of the selected models. These values can be seen in table 3. From the model predictions, the BTR Tucker and FTR CP models perform best, though it is important to note that these two models produce coefficient estimates that are very close to zero, further suggesting that there may be very low signal in the dataset for

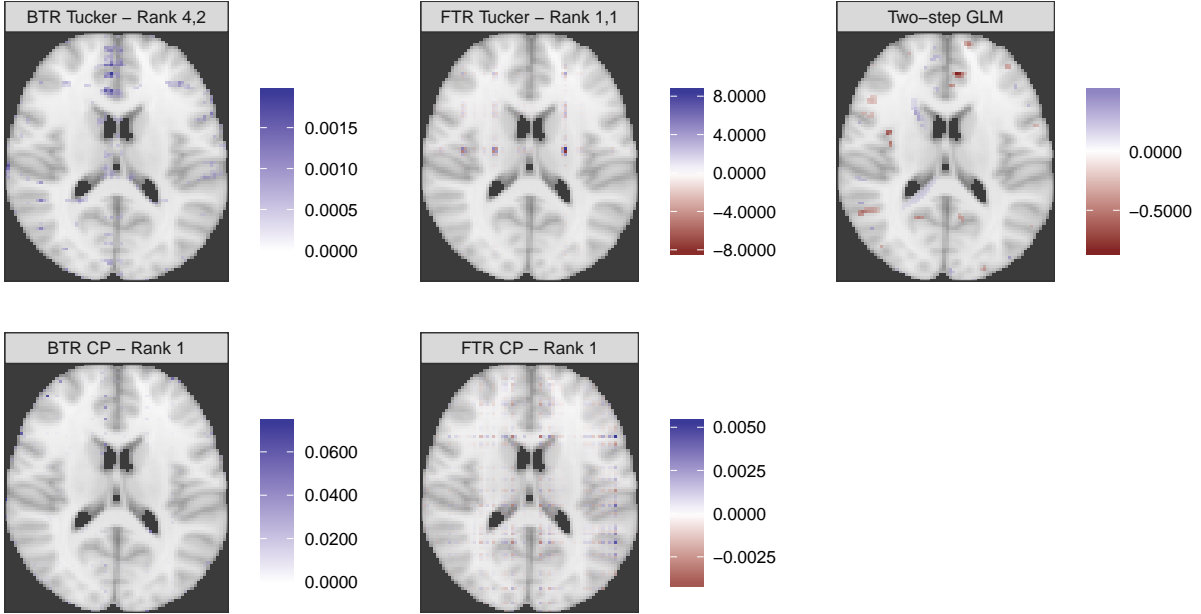


Figure 5: Point estimates for the coefficients in the 45th axial slice of the ADNI data training subset.

Model	RMSPE	Pearson	$\gamma_{\text{Edu}}$ (95% Cred. Int.)	$\gamma_{\text{APOE4}}$ (95% Cred. Int.)
BTR Tucker - Rank 4,2	2.752	0.236	0.135 (-0.709,1.073)	-0.814 (-1.546,0.127)
BTR CP - Rank 1	2.772	0.220	0.084 (-1.274,1.031)	-0.842 (-1.839,0.126)
FTR Tucker - Rank 1,1	4.438	0.029	0.074	-0.953
FTR CP - Rank 1	2.761	0.215	0.04	-0.914
Two-step GLM	161.308	0.057	0.04	-0.914
No-image	2.762	0.213	0.04	-0.914

Table 3: The root mean squared prediction error, Pearson correlation for predictions in the test data, and the final point estimates of the non-tensor coefficients for the selected competitor models.

a significant association between the MMSE and the 45th axial slice of the structural MRI scan.

## 5 Discussion

The Bayesian tensor regression using the Tucker decomposition shows improvement over other tensor regression methods within simulation studies, under the assumption of normally distributed error. Through simulation tests, it is shown that the BTR Tucker models slightly outperform the frequentist Tucker tensor regression models, and it more drastically outperform the Bayesian tensor regression competitor models based on the CP/PARAFAC tensor decomposition. These performance improvements are seen in the inference for both the tensor-valued coefficients, and the vector-valued coefficients.

In the analysis of the ADNI data, it was found that all of the different competing models resulted in

an inconclusive final inference about the voxels within the axial slice that show significant correlations with the MMSE scores. Comparing the predictions made with the test data show that the BTR Tucker model outperforms the BTR CP model, if only because it shrinks values in the tensor coefficient to zero.

Future extensions of this model that are planned include using expectation-maximization or variational algorithms to rapidly determine point estimates and select for optimal ranks for a full Markov chain Monte Carlo posterior distribution simulation. These methods would enhance the analysis while speeding it up considerably. Additionally, formalizing the software used in these and other Bayesian tensor regression methods is a priority, in order to make these analyses accessible to neuroimagers that have not been formally trained in Bayesian statistical modeling.

## References

Artin Armagan, David B Dunson, and Jaeyong Lee. Generalized double pareto shrinkage. *Statistica Sinica*, 23(1):119, 2013.

Yoav Benjamini and Yosef Hochberg. Controlling the false discovery rate: a practical and powerful approach to multiple testing. *Journal of the Royal statistical society: series B (Methodological)*, 57(1):289–300, 1995.

Eyal Bercovich and Marcia C Javitt. Medical imaging: From roentgen to the digital revolution, and beyond. *Rambam Maimonides medical journal*, 9(4), 2018.

Michael A Bruno, Eric A Walker, and Hani H Abujudeh. Understanding and confronting our mistakes: the epidemiology of error in radiology and strategies for error reduction. *Radiographics*, 35(6):1668–1676, 2015.

Anders Eklund, Thomas E Nichols, and Hans Knutsson. Cluster failure: Why fMRI inferences for spatial extent have inflated false-positive rates. *Proceedings of the national academy of sciences*, 113(28):7900–7905, 2016.

Karl J Friston, John Ashburner, Christopher D Frith, J-B Poline, John D Heather, and Richard SJ Frackowiak. Spatial registration and normalization of images. *Human brain mapping*, 3(3):165–189, 1995.

Rajarshi Guhaniyogi, Shaan Qamar, and David B Dunson. Bayesian tensor regression. *The Journal of Machine Learning Research*, 18(1):2733–2763, 2017.

Mark Jenkinson and Stephen Smith. A global optimisation method for robust affine registration of brain images. *Medical image analysis*, 5(2):143–156, 2001.

Mark Jenkinson, Peter Bannister, Michael Brady, and Stephen Smith. Improved optimization for the robust and accurate linear registration and motion correction of brain images. *Neuroimage*, 17(2):825–841, 2002.

Hanning Li and Debdeep Pati. Variable selection using shrinkage priors. *Computational Statistics & Data Analysis*, 107:107–119, 2017.

Xiaoshan Li, Da Xu, Hua Zhou, and Lexin Li. Tucker tensor regression and neuroimaging analysis. *Statistics in Biosciences*, 10(3):520–545, 2018.

Martin A Lindquist and Amanda Mejia. Zen and the art of multiple comparisons. *Psychosomatic medicine*, 77(2):114, 2015.

John Muschelli, Elizabeth Sweeney, Martin Lindquist, and Ciprian Crainiceanu. *fslr*: Connecting the fsl software with r. *The R Journal*, 7(1):163–175, 2015.

Sean M Nestor, Raul Rupsingh, Michael Borrie, Matthew Smith, Vittorio Accomazzi, Jennie L Wells, Jennifer Fogarty, Robert Bartha, and Alzheimer’s Disease Neuroimaging Initiative. Ventricular enlargement as a possible measure of alzheimer’s disease progression validated using the alzheimer’s disease neuroimaging initiative database. *Brain*, 131(9):2443–2454, 2008.

Verna C Pangman, Jeff Sloan, and Lorna Guse. An examination of psychometric properties of the mini-mental state examination and the standardized mini-mental state examination: implications for clinical practice. *Applied Nursing Research*, 13(4):209–213, 2000.

William D Penny, Karl J Friston, John T Ashburner, Stefan J Kiebel, and Thomas E Nichols. *Statistical parametric mapping: the analysis of functional brain images*. Elsevier, 2011.

Fast robust automated brain extraction Smith. Human brain mapping-wiley online library, 2002.

Warren J Strittmatter and Allen D Roses. Apolipoprotein e and alzheimer’s disease. *Annual review of neuroscience*, 19(1):53–77, 1996.

Robert Tibshirani. Regression shrinkage and selection via the lasso. *Journal of the Royal Statistical Society: Series B (Methodological)*, 58(1):267–288, 1996.

Ledyard R Tucker. Some mathematical notes on three-mode factor analysis. *Psychometrika*, 31(3):279–311, 1966.

Marijke Welvaert, Joke Durnez, Beatrijs Moerkerke, Geert Verdoollaeghe, and Yves Rosseel. neuRosim: An R package for generating fmri data. *Journal of Statistical Software*, 44(10):1–18, 2011. URL <http://www.jstatsoft.org/v44/i10/>.

Hua Zhou, Lexin Li, and Hongtu Zhu. Tensor regression with applications in neuroimaging data analysis. *Journal of the American Statistical Association*, 108(502):540–552, 2013.

## A Model

$$\begin{aligned}
y_i &= \langle \mathbf{B}, \mathbf{X}_i \rangle + \boldsymbol{\gamma} \boldsymbol{\eta}_i + \epsilon_i \\
\epsilon_i &\sim N(0, \sigma_y^2) \\
\sigma_y^2 &\sim \text{Inverse Gamma} \left( \frac{\nu}{2}, \frac{\nu}{2} s_0^2 \right) \\
\mathbf{B} &= \sum_{r_1=1}^{R_1} \cdots \sum_{r_D=1}^{R_D} \boldsymbol{\beta}_{1,r_1} \circ \cdots \circ \boldsymbol{\beta}_{D,r_D} \\
\boldsymbol{\beta}_{j,r_j} &\sim N(\mathbf{0}, \tau \phi_{j,r_j} \mathbf{W}_{j,r_j}), \quad \mathbf{W} \text{ is a diagonal matrix} \\
\tau &\sim \text{Gamma}(a_\tau, b_\tau) \\
\text{for } r_j < R_j, \quad \phi_{j,r_j} &= \pi_{j,r_j} \prod_{\ell=1}^{r_j-1} (1 - \pi_{j,\ell}) \\
\phi_{j,R_j} &= 1 - \sum_{r_j=1}^{R_j-1} \phi_{j,r_j} \\
\pi_{j,r_j} &\sim \text{Beta}(1, \alpha) \\
\text{for } \omega_{j,r_j, \ell} \in \mathbf{W}_{j,r_j}, \quad \omega_{j,r_j, \ell} &\sim \text{Exp} \left( \frac{\lambda_{j,r_j}^2}{2} \right) \\
\lambda_{j,r_j} &\sim \text{Gamma}(a_\lambda, b_\lambda) \\
\boldsymbol{\gamma} &\sim N(\boldsymbol{\mu}_\gamma, \boldsymbol{\Sigma}_\gamma)
\end{aligned}$$

## B Posterior Full Conditional Distributions

### B.1 $\sigma_y^2$

$$\begin{aligned}
p(\sigma_y^2 | \mathbf{y}, \mathbf{B}, \mathbf{X}, \boldsymbol{\gamma}, \boldsymbol{\eta}) &\propto (\sigma_y^2)^{-(a_\sigma + N/2) - 1} \exp \left\{ -\frac{1}{\sigma_y^2} \left( b_\sigma + \frac{1}{2} \sum_{i=1}^N (y_i - \langle \mathbf{B}, \mathbf{X}_i \rangle - \boldsymbol{\gamma}' \boldsymbol{\eta}_i)^2 \right) \right\} \\
\sigma_y^2 | \mathbf{y}, \mathbf{B}, \mathbf{X}, \boldsymbol{\gamma}, \boldsymbol{\eta} &\sim \text{Inverse Gamma} \left( a_\sigma + \frac{N}{2}, b_\sigma + \frac{1}{2} \sum_{i=1}^N (y_i - \langle \mathbf{B}, \mathbf{X}_i \rangle - \boldsymbol{\gamma}' \boldsymbol{\eta}_i)^2 \right)
\end{aligned}$$

### B.2 $\boldsymbol{\gamma}$

First, set  $\tilde{y}_i = y_i - \langle \mathbf{B}, \mathbf{X}_i \rangle$ .

$$\begin{aligned}
p(\gamma | \mathbf{y}, \mathbf{B}, \mathbf{X}, \boldsymbol{\eta}, \sigma_y^2, \mathbf{V}) &\propto \exp \left\{ -\frac{1}{2} \gamma' \left( \mathbf{V}^{-1} + \frac{1}{\sigma_y^2} \mathbf{I} \right) \gamma - \frac{1}{\sigma_y^2} ((\gamma' \boldsymbol{\eta})' \tilde{\mathbf{y}}) - \frac{1}{\sigma_y^2} (\tilde{\mathbf{y}}' (\gamma' \boldsymbol{\eta})) \right\} \\
\gamma | \mathbf{y}, \mathbf{B}, \mathbf{X}, \boldsymbol{\eta}, \sigma_y^2, \mathbf{V} &\sim N \left( \left( \mathbf{V}^{-1} + \frac{1}{\sigma_y^2} \mathbf{I} \right)^{-1} \frac{\boldsymbol{\eta}' \tilde{\mathbf{y}}}{\sigma_y^2}, \left( \mathbf{V}^{-1} + \frac{1}{\sigma_y^2} \mathbf{I} \right)^{-1} \right)
\end{aligned}$$

### B.3 $\boldsymbol{\beta}_{j,r_j}$

First, call  $\tilde{\mathbf{B}} = \mathbf{B} \setminus \boldsymbol{\beta}_{j,r_j}$ , and  $\mathbf{B}^* = \mathbf{B} \ni \boldsymbol{\beta}_{j,r_j}$ . Then,

$$y_i = \langle \mathbf{B}^* + \tilde{\mathbf{B}}, \mathbf{X}_i \rangle + \gamma' \boldsymbol{\eta}_i + \epsilon_i.$$

Next, set

$$\tilde{y}_i = y_i - \gamma' \boldsymbol{\eta}_i - \langle \tilde{\mathbf{B}}, \mathbf{X}_i \rangle.$$

Define the *mode-k matricization*  $\mathbf{X}_{(j)}$  of an array  $\mathbf{X} \in \mathbb{R}^{p_1 \times p_2 \times \dots \times p_D}$  to be  $\mathbf{X}_{(j)} \in \mathbb{R}^{p_j \times p_1 p_2 \dots p_{j-1} p_{j+1} \dots p_D}$ .

Set the  $\mathbf{B}_{-j}^*$  as the tensor composition of all  $\boldsymbol{\beta}_{\ell,r_\ell}$  such that  $\ell \in \{1, 2, \dots, D\} \setminus j$ , which has dimension  $D-1$ .

Finally using the following notation:

$$\tilde{\mathbf{y}} = \begin{pmatrix} \tilde{y}_1 \\ \vdots \\ \tilde{y}_N \end{pmatrix}, \quad \mathbf{X}^* = \begin{pmatrix} \mathbf{X}_{1(j)} \mathbf{B}_{-j}^* \\ \vdots \\ \mathbf{X}_{N(j)} \mathbf{B}_{-j}^* \end{pmatrix},$$

the posterior full conditional distribution for  $\boldsymbol{\beta}_{j,r_j}$  can be written as

$$\begin{aligned}
\boldsymbol{\beta}_{j,r_j} | \mathbf{y}, \mathbf{X}, \sigma_y^2, \tau, \phi_{j,r_j}, \mathbf{W}_{j,r_j} &\sim \\
N \left( \left( \frac{1}{\tau \phi_{j,r_j}} \mathbf{W}_{j,r_j}^{-1} + \frac{1}{\sigma_y^2} \mathbf{X}^{*'} \mathbf{X}^* \right)^{-1} \frac{\tilde{\mathbf{y}}' \mathbf{X}^*}{\sigma_y^2}, \left( \frac{1}{\tau \phi_{j,r_j}} \mathbf{W}_{j,r_j}^{-1} + \frac{1}{\sigma_y^2} \mathbf{X}^{*'} \mathbf{X}^* \right)^{-1} \right)
\end{aligned}$$

### B.4 $\tau$

$$p(\tau | a_\tau, b_\tau, \boldsymbol{\phi}, \mathbf{W}, \mathbf{B}) \propto \tau^{a_\tau - \frac{1}{2} \sum_{j=1}^D R_j p_j - 1} e^{-b_\tau \tau - \frac{1}{2\tau} \sum_{j=1}^D \sum_{r_j=1}^{R_j} \frac{1}{\phi_{j,r_j}} \boldsymbol{\beta}'_{j,r_j} \mathbf{W}_{j,r_j}^{-1} \boldsymbol{\beta}_{j,r_j}}$$

$$\tau | a_\tau, b_\tau, \boldsymbol{\phi}, \mathbf{W}, \mathbf{B} \sim \text{Generalized Inverse Gaussian} \left( a_\tau - \frac{1}{2} \sum_{j=1}^D R_j p_j, 2b_\tau, \sum_{j=1}^D \sum_{r_j=1}^{R_j} \frac{1}{\phi_{j,r_j}} \boldsymbol{\beta}'_{j,r_j} \mathbf{W}_{j,r_j}^{-1} \boldsymbol{\beta}_{j,r_j} \right)$$

### B.5 $\pi_{j,r_j}$

$$p(\pi_{j,r_j} | -) \propto \pi_{j,r_j}^{-p_j/2} (1 - \pi_{j,r_j})^{\alpha - (R_j - r_j)p_j/2 - 1} \exp \left\{ -\frac{1}{\tau} \left[ \frac{1}{\pi_{j,r_j}} \left( \boldsymbol{\beta}'_{j,r_j} \mathbf{W}_{j,r_j}^{-1} \boldsymbol{\beta}_{j,r_j} \right) \right. \right. \\ \left. \left. + \sum_{k=r_j+1}^{R_j} \frac{1}{\pi_{j,k} \prod_{\ell=r_j}^{k-1} (1 - \pi_{j,\ell})} \left( \boldsymbol{\beta}'_{j,k} \mathbf{W}_{j,k}^{-1} \boldsymbol{\beta}_{j,k} \right) \right] \right\}$$

### B.6 $\omega_{j,r_j,\ell}$

$$p(\omega_{j,r_j,\ell} | \beta_{j,r_j,\ell}, \tau, \phi_{j,r_j}) \propto \omega_{j,r_j,\ell}^{-1/2} e^{-\frac{1}{2} \left( \lambda_{j,r_j}^2 \omega_{j,r_j,\ell} + \frac{\beta_{j,r_j,\ell}^2}{\tau \phi_{j,r_j} \omega_{j,r_j,\ell}} \right)} \\ \omega_{j,r_j,\ell} | \beta_{j,r_j,\ell}, \tau, \phi_{j,r_j} \sim \text{Generalized Inverse Gaussian} \left( \frac{1}{2}, \lambda_{j,r_j}^2, \frac{\beta_{j,r_j,\ell}^2}{\tau \phi_{j,r_j}} \right)$$

### B.7 $\lambda_{j,r_j}$

In order to find a posterior full conditional distribution in a closed form for  $\lambda_{j,r_j}$ ,  $\omega_{j,r_j,\ell}$  must be integrated out of the prior for  $\beta_{j,r_j,\ell}$ .

$$\int_0^\infty \frac{1}{\sqrt{2\pi\tau\phi_{j,r_j}\omega_{j,r_j,\ell}}} \exp \left\{ -\frac{\beta_{j,r_j,\ell}^2}{2\tau\phi_{j,r_j}\omega_{j,r_j,\ell}} \right\} \frac{\lambda_{j,r_j}^2}{2} \exp \left\{ -\frac{1}{2}\lambda_{j,r_j}^2 \omega_{j,r_j,\ell} \right\} d\omega_{j,r_j,\ell} \\ = \frac{\lambda_{j,r_j}}{2(\tau\phi_{j,r_j})^{-1/2}} \exp \left\{ -\frac{\lambda_{j,r_j} |\beta_{j,r_j,\ell}|}{(\tau\phi_{j,r_j})^{-1/2}} \right\}$$

$$p(\lambda_{j,r_j} | \boldsymbol{\beta}_{j,r_j}, \tau, \phi_{j,r_j}) \propto \lambda_{j,r_j}^{a_\lambda - 1} \exp \left\{ -b_\lambda \lambda_{j,r_j} \right\} \times \prod_{\ell=1}^{p_j} \lambda_{j,r_j} \exp \left\{ -\frac{\lambda_{j,r_j} |\beta_{j,r_j,\ell}|}{(\tau\phi_{j,r_j})^{1/2}} \right\} \\ \lambda_{j,r_j} | \boldsymbol{\beta}_{j,r_j}, \tau, \phi_{j,r_j} \sim \text{Gamma} \left( a_\lambda + p_j, b_\lambda + \frac{\sum |\beta_{j,r_j,\ell}|}{(\tau\phi_{j,r_j})^{1/2}} \right)$$